



# Cobalt doped ceria for abundant storage of surface active oxygen and efficient elemental mercury oxidation in coal combustion flue gas

Weichun Yang<sup>a</sup>, Chaofang Li<sup>a</sup>, Haiying Wang<sup>a</sup>, Xingyao Li<sup>a</sup>, Weilin Zhang<sup>b</sup>, Hailong Li<sup>b,\*</sup>

<sup>a</sup> Chinese National Engineering Research Center for Control & Treatment of Heavy Metal Pollution, Institute of Environmental Engineering, School of Metallurgy and Environment, Central South University, Changsha, Hunan, China

<sup>b</sup> School of Energy Science and Engineering, Central South University, Changsha, Hunan, China

## ARTICLE INFO

### Keywords:

Mercury oxidation  
Surface active oxygen  
Cobalt doped ceria  
Coal combustion

## ABSTRACT

Cobalt doped CeO<sub>2</sub> (Co-CeO<sub>2</sub>) prepared by a single-step hydrothermal method was used for Hg<sup>0</sup> catalytic oxidation. The catalysts were characterized by scanning electron microscope, transmission electron microscope, X-ray diffraction, Raman spectroscopy, electron paramagnetic resonance, X-ray photoelectron spectroscopy, H<sub>2</sub>-temperature programmed reduction test, and thermogravimetric measurement. The results show that the exposed planes for the flake-shaped Co-CeO<sub>2</sub> mainly were (110) and (100) with low oxygen vacancy formation energies. Abundant oxygen vacancy defects were identified on the Co-CeO<sub>2</sub>, which further induced plentiful chemisorbed oxygen on the surface. The oxygen storage capacity for the Co-CeO<sub>2</sub> was up to 1.43 μmol O<sub>2</sub> m<sup>-2</sup> at 200 °C, and a large portion of this capacity was for chemisorbed oxygen. Without the introduction of gas-phase O<sub>2</sub>, Hg<sup>0</sup> oxidation probably occurred through a Mars-Maessen mechanism, where active chemisorbed oxygen originated from oxygen vacancy defects reacts with adsorbed Hg<sup>0</sup> to form HgO. Active chlorine species was generated from the interactions of chemisorbed oxygen with trace amount gaseous HCl. The active chlorine compensated the slight inhibitive effects of SO<sub>2</sub> and H<sub>2</sub>O, leading to above 90% Hg<sup>0</sup> oxidation under simulated low-rank coal burning flue gas atmosphere at a gas hourly space velocity of 160,000 h<sup>-1</sup>. The abundant active chemisorbed oxygen played important role in and guaranteed an efficient Hg<sup>0</sup> oxidation in extremely adverse application environment. These results reveal the role of doping metals on structure-catalytic property relations for CeO<sub>2</sub>, which opened a new strategy for controlling mercury emission from coal-fired flue gas using CeO<sub>2</sub> based catalysts by tuning the morphology and exposed planes.

## 1. Introduction

Coal combustion was the significant anthropogenic atmospheric mercury source [1]. With the Minamata Convention on Mercury, aiming to avoid the harmful of mercury for human health and the environment, took effect on 16 August 2017, more and more attentions have been paid on reducing mercury emission from coal-burning flue gas. Before that, strict standards were applied in China and the United States for mercury emission restriction from coal combustion power plants [2]. To meet the international convention and national mercury emission standards, effective mercury removal techniques are urgently needed [3,4].

Three forms of mercury co-exist in coal combustion flue gas, i.e., elemental mercury (Hg<sup>0</sup>), oxidized mercury (Hg<sup>2+</sup>), and particulate-bound mercury (Hg<sup>p</sup>) [5]. Gaseous Hg<sup>0</sup> endures as the main form of mercury emitted from the stack to the environment due to its high

volatility and insolubility [6]. In contrast, Hg<sup>2+</sup> can be concurrently removed in the particulate matter control devices and wet flue gas desulfurization systems, with particulate matters and acid gases, respectively. However, the transformation of Hg<sup>0</sup> to Hg<sup>2+</sup> in flue gas is kinetically limited, and the rate of homogeneous Hg<sup>0</sup> oxidation was generally slow [7]. Therefore, catalysts able to efficiently (80%) convert Hg<sup>0</sup> to Hg<sup>2+</sup> would have great value in economically controlling mercury emission from coal-burning flue gas [8,9].

Metal oxide-based catalysts were widely reported to facilitate Hg<sup>0</sup> oxidation [7,10,11]. The dominant Hg<sup>0</sup> oxidation reaction on metal oxides was believed to be that Hg<sup>0</sup> reacts with hydrogen chloride (HCl) and oxygen to form volatile mercuric chloride [12]. HCl was proved to play an important role in Hg<sup>0</sup> oxidation [13]. However, because HCl is already at a fully reduced state, it cannot oxidize Hg<sup>0</sup> directly. Therefore, oxygen is indispensable for the reactions between Hg<sup>0</sup> and HCl over metal oxides based catalysts. Other than gas-phase O<sub>2</sub>, catalyst

\* Corresponding author.

E-mail address: [hailongli18@gmail.com](mailto:hailongli18@gmail.com) (H. Li).

<https://doi.org/10.1016/j.apcatb.2018.08.014>

Received 2 April 2018; Received in revised form 2 August 2018; Accepted 4 August 2018

Available online 06 August 2018

0926-3373/ © 2018 Elsevier B.V. All rights reserved.

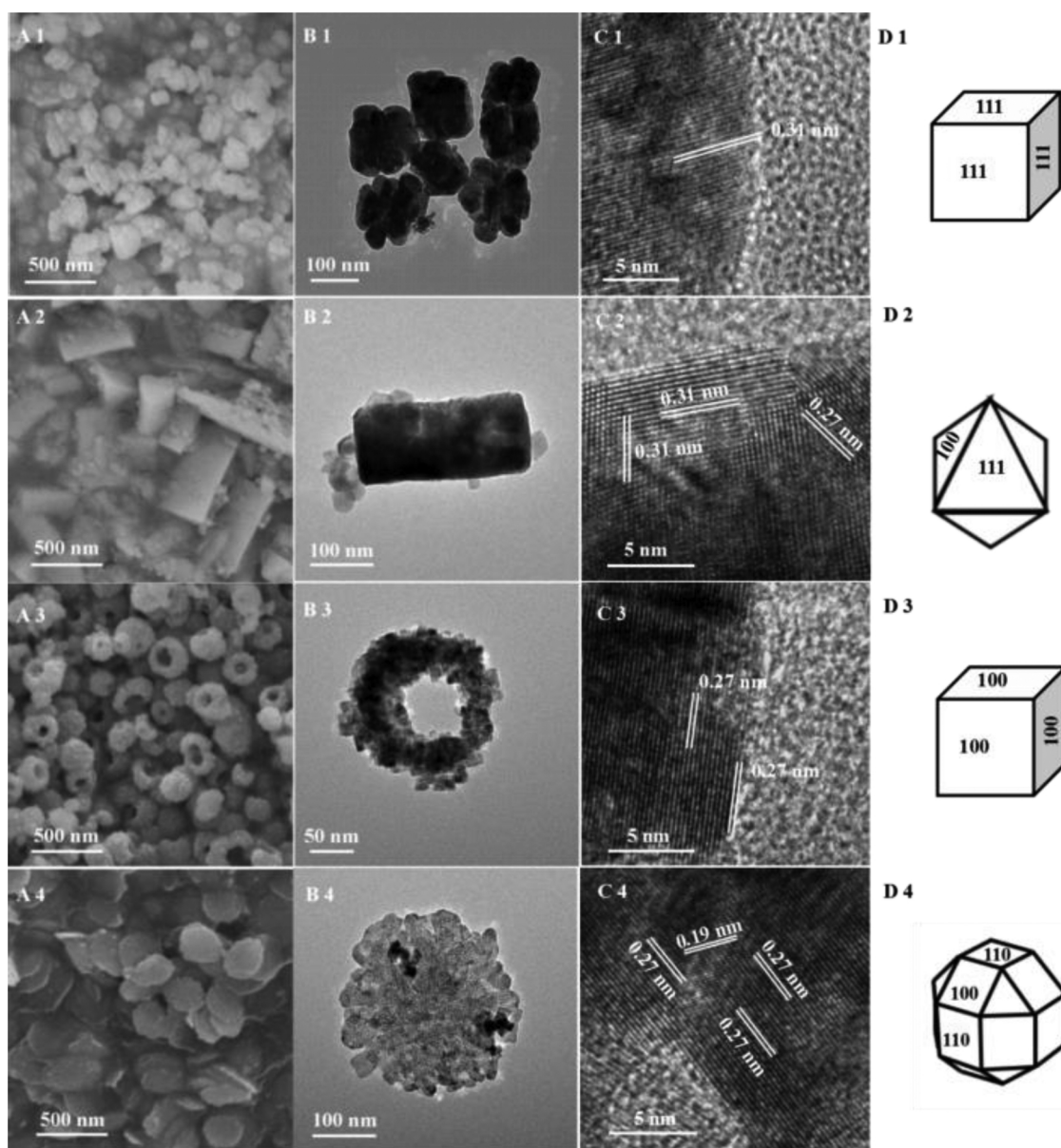


**Fig. 1.** SEM images (A), TEM images (B), HRTEM images (C), and schematic illustrations (D) of: pure CeO<sub>2</sub> (A1, B1, C1, D1), Fe-CeO<sub>2</sub> (A2, B2, C2, D2), Cu-CeO<sub>2</sub> (A3, B3, C3, D3), and Co-CeO<sub>2</sub> (A4, B4, C4, D4).

**Table 1**  
Elemental composition and structural parameters for the samples.

Sample	Ce (wt%) <sup>a</sup>	M (wt%) <sup>a</sup>	Lattice parameter (nm) <sup>b</sup>	Average crystallite size (nm) <sup>b</sup>	S <sub>BET</sub> (m <sup>2</sup> g <sup>-1</sup> ) <sup>c</sup>	Average pore diameter (nm) <sup>c</sup>	Pore volume (cm <sup>3</sup> g <sup>-1</sup> ) <sup>c</sup>
Pure CeO <sub>2</sub>	80.4	–	0.540	9.77	90.71	14.13	0.140
Fe-CeO <sub>2</sub>	67.9	8.81	0.538	8.90	55.21	15.74	0.057
Cu-CeO <sub>2</sub>	78.2	1.40	0.541	9.43	95.11	8.28	0.157
Co-CeO <sub>2</sub>	69.4	7.64	0.538	8.99	65.22	10.01	0.111

<sup>a</sup> From ICP analysis, M represents Fe, Cu or Co.

<sup>b</sup> From XRD analysis. Lattice parameter is calculated in the MDI jade software and average crystallite size is obtained by Scherrer's formula.

<sup>c</sup> From N<sub>2</sub> adsorption-desorption measurement. S<sub>BET</sub> presents BET specific surface area.

stored oxygen, particularly the surface chemisorbed oxygen, is more active for several oxidation processes [5,14]. Therefore, we hypothesize that catalyst possessing large oxygen storage capacity (OSC) is beneficial for oxidizing elemental mercury, and likely allowing a steady oxidation process of elemental mercury in insufficient or no oxygen environment, for example with low excess air combustion.

Taking advantage of the active facile Ce<sup>3+</sup>/Ce<sup>4+</sup> redox cycle and the corresponding superior OSC, ceria and its polymetallic oxides has been investigated as promoters for Hg<sup>0</sup> oxidation [8,15–17]. However, these studies focused on Hg<sup>0</sup> oxidation performance and the potential practical application of these ceria-based catalysts, but neglected the relationship between structure, morphology, OSC, and the catalytic

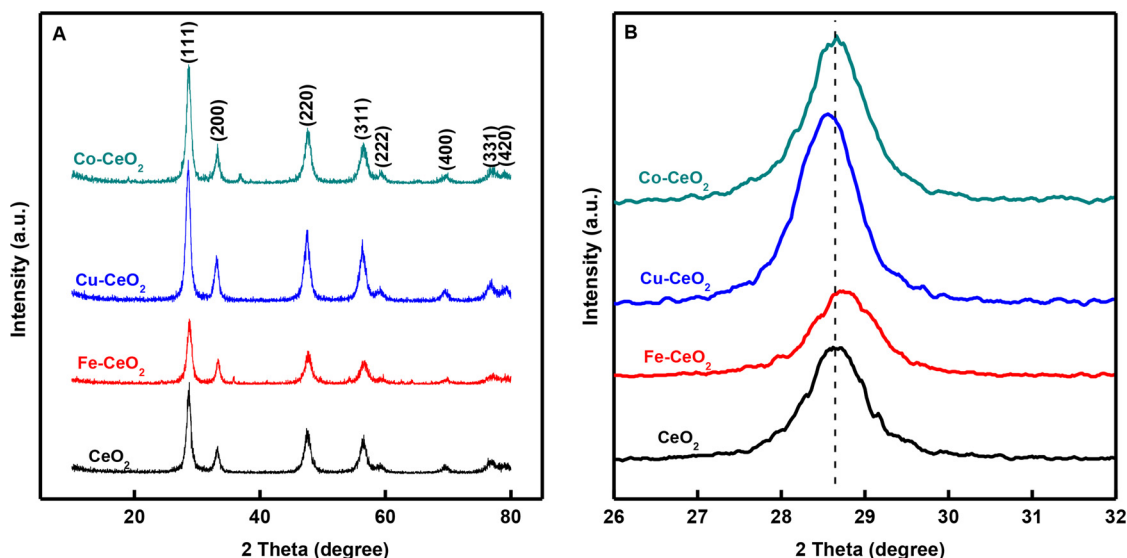


Fig. 2. XRD patterns (A) and the magnified peak {111} (B) for pure  $\text{CeO}_2$ ,  $\text{Fe-CeO}_2$ ,  $\text{Cu-CeO}_2$ , and  $\text{Co-CeO}_2$ .

activity of catalysts. Actually, catalysts with different structure and shape usually exhibit great variation in catalytic performances. For example,  $\text{CeO}_2$  nanocrystals with rodlike and cubelike shapes displayed higher OSC and exhibited higher CO conversion at lower temperature than spheroidal particles [18]. Due to the nanorod surface structures and the high OSC,  $\text{CeO}_2$  nanorods with 5–7 nm diameter exhibited excellent low temperature catalytic performance [19]. The shape of  $\text{CeO}_2$  nanocrystal is correlated with the surface structures and exposed crystal planes, which exhibit different energies for generating oxygen vacancy [20]. The energies for generating oxygen vacancy on (110) and (100) planes were reported to be lower than that on (111) [21,22]. Therefore, it is very possible that  $\text{CeO}_2$  crystals with more exposed (110) and (100) planes would facilitate to form oxygen vacancies, and hence lead to greater OSC and better catalytic performance in  $\text{Hg}^0$  oxidation.

Doping foreign metal ions, especially those with smaller radii, into  $\text{CeO}_2$  lattice was identified to be an efficient approach for controlling the nucleation/growth of  $\text{CeO}_2$  crystal, thus the exposed planes, shape of the  $\text{CeO}_2$ . Liu et al. reported that the  $\text{Cu}^{2+}$  doping could induce acceleration in the nucleation to control the size of the doped ceria and further assisted Ostwald ripening occurring in the solvothermal reaction to get  $\text{CeO}_2$  nanospheres with different hollowness [23]. Guo et al. obtained  $\text{CeO}_2$  with uniform 2D disklike nanostructures by doping cobalt to assist the oriented attachment process along (110) planes [24]. Moreover, the doped  $\text{CeO}_2$  often exhibits greatly enhanced catalytic activity in oxidation processes. For instance, introduction of  $\text{Zr}^{4+}$ ,  $\text{Hf}^{4+}$ ,  $\text{La}^{3+}$ ,  $\text{Pr}^{3+}$ ,  $\text{Fe}^{3+}$ ,  $\text{Mn}^{2+}$  ions into the ceria catalysts promoted their soot oxidation activities [25]. The incorporating of  $\text{Co}^{2+}$  (0.65 Å) into  $\text{CeO}_2$  crystal also resulted in superior catalytic activities for the oxidation of CO [24,26],  $\text{N}_2\text{O}$ , volatile organic compounds (VOCs), and propene [27]. It was believed that the structural distortion of these  $\text{Co}^{2+}$  doped ceria made more (110) and (100) planes exposed, which decreased the oxygen vacancies formation energy, and hence led to greater OSC and superior catalytic performance [28]. Therefore, it is reasonable to hypothesize that  $\text{Co}^{2+}$  doped ceria would be a superior catalyst for  $\text{Hg}^0$  oxidation.

In present study, cobalt doped  $\text{CeO}_2$  nanocrystal was prepared through a single-step hydrothermal method and used for oxidizing  $\text{Hg}^0$  in simulated coal combustion flue gases. To clarify the involved structural-catalytic property relations for ceria nanomaterials, pure  $\text{CeO}_2$ ,  $\text{Fe}^{3+}$  (0.64 Å),  $\text{Cu}^{2+}$  (0.73 Å) doped  $\text{CeO}_2$  were also prepared and systematically investigated.

## 2. Experimental

### 2.1. Catalyst preparation

A single-step hydrothermal method was applied to prepare the nanosized pure  $\text{CeO}_2$  and  $\text{CeO}_2$  nanocomposites. For the  $\text{CeO}_2$  nanocomposites, 1 mmol of  $\text{Ce}(\text{NO}_3)_3 \cdot 6\text{H}_2\text{O}$  (analytical grade, Aldrich), 0.4 mmol of metal precursor ( $\text{FeCl}_3 \cdot 6\text{H}_2\text{O}$ ,  $\text{CuCl}_2 \cdot 2\text{H}_2\text{O}$ , or  $\text{CoCl}_2 \cdot 6\text{H}_2\text{O}$ , analytical grade, Sinopharm) and 0.5 g of polyvinylpyrrolidone (K30, analytical grade, Sinopharm) were dissolved in 30 mL deionized water and mixed together with vigorous stirring until the forming of a clear solution. After added proper amounts of urea (analytical grade, Sinopharm) and stirred for 30 min, the solution was placed at a 100 mL autoclave for 10 h at 150 °C. The final products were filtered and washed with distilled water and ethanol (99%, Sinopharm) for three times. After dried overnight at 60 °C and calcined at 500 °C in air for 4 h, nanoscale doped cerium oxide-based nanomaterials were obtained. The as-prepared samples were denoted as  $\text{Fe-CeO}_2$ ,  $\text{Cu-CeO}_2$  and  $\text{Co-CeO}_2$ , respectively. The pure  $\text{CeO}_2$  was fabricated following the same process without adding the metal precursor.

### 2.2. Catalyst characterization

The crystallinities of the samples were measured using an X-ray powder diffraction (XRD) spectra (D/MAX 2500 VB + XX diffractometer), with a Cu-K $\alpha$  radiation ( $\lambda = 0.15406$  nm), operating in the range of 10–80° (2 $\theta$ ). Scanning electron microscope (SEM, JSM-6360) and transmission electron microscope (TEM, TECNAI G2 F20, accelerating voltage = 200 kV) were used to analyze the morphology. The elements distributions were characterized by an energy-dispersive spectroscopy (EDS) equipped with the TEM. The software used for digital image analysis and crystallographic indexation was Digital Micrgraph. The BET surface area and textural properties of the samples were determined by a  $\text{N}_2$  adsorption-desorption isotherms measured on a nitrogen adsorption apparatus (ASAP 2020). Coupled plasma atomic emission spectroscopy (ICP-AES, IRIS Intrepid II XSP, Thermo Electron Corporation) was applied to measure the content of doping metal in materials. The materials were digested by aqua regia at 90 °C for two days. A Via Reflex Raman spectrometer with 532 nm emission line from Ar $^{+}$  laser were used to obtain Raman spectra under ambient conditions. Electron paramagnetic resonance (EPR) measurements were carried out on a Bruker E500 spectrometer. X-ray photoelectron spectroscopy (XPS)



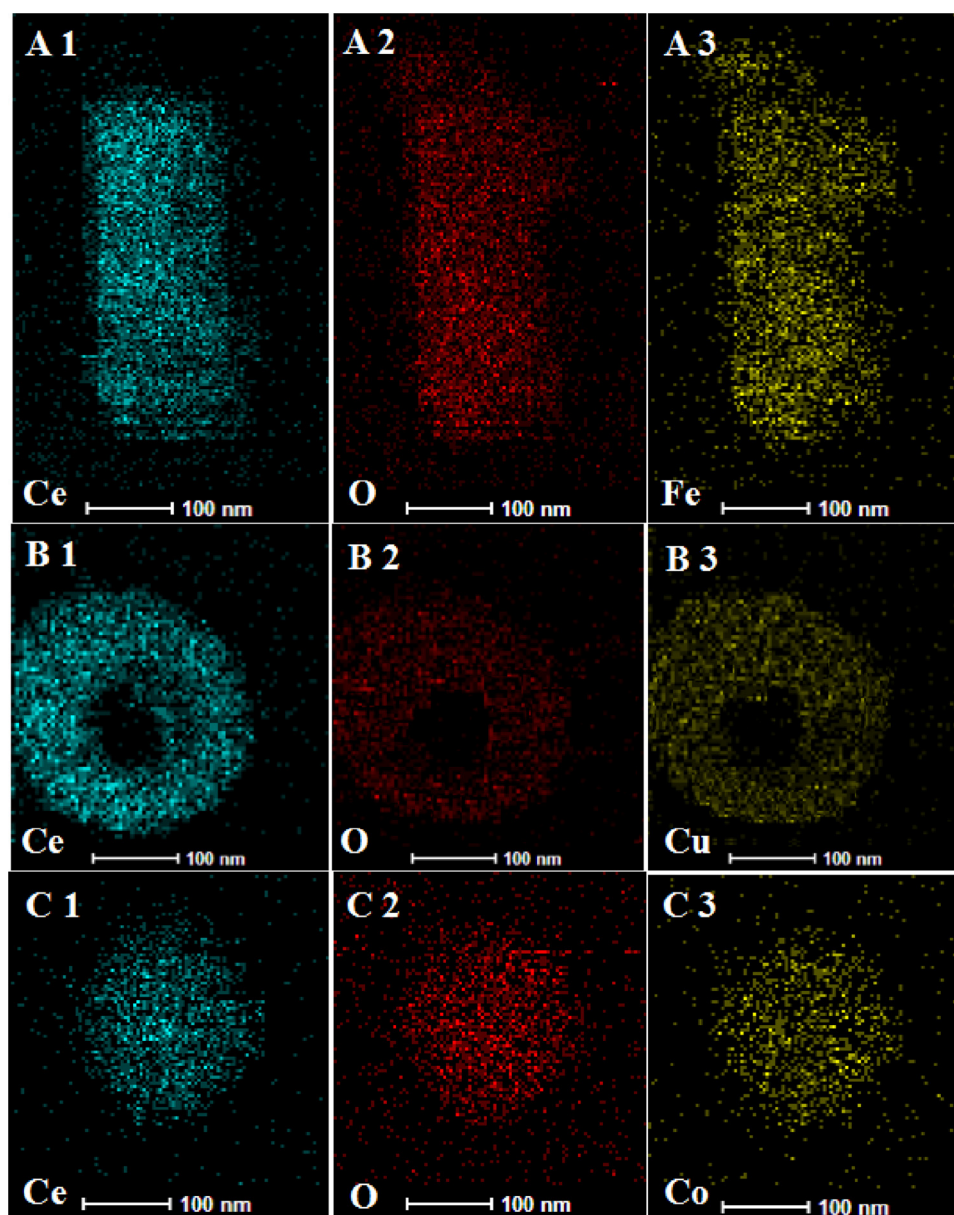


Fig. 3. EDS element mapping of: Fe-CeO<sub>2</sub> (A), Cu-CeO<sub>2</sub> (B), and Co-CeO<sub>2</sub> (C).

measurements were recorded (Thermo Fisher Scientific K-Alpha 1063) using Al K $\alpha$  radiation as the X-ray source. All binding energies were calibrated by the C 1s peak at 284.8 eV.

The H<sub>2</sub>-temperature programmed reduction (H<sub>2</sub>-TPR) was carried out on PCA-1200 (Bjbuilder, Beijing). Typically, to avoid the influence of the adsorbed water and impurities, the catalyst was pretreated under Ar atmosphere at 120 °C for 30 min. After cooling down to 30 °C, a 7 vol % H<sub>2</sub>-Ar gas (30 mL min<sup>-1</sup>) was introduced into the reaction equipment. The temperature was finally arrived to 900 °C and the heating rate was 10 °C min<sup>-1</sup>. OSC of the Co-CeO<sub>2</sub> catalyst was measured by thermogravimetric (TG) method. A repeated thermal treatment was carried out on the SETSYS Evolution thermo analyzer in 200 °C. About 15 mg Co-CeO<sub>2</sub> was used and the temperature was raised to 200 °C and kept for 1 h in Ar environment to stabilize the airstream, then 2% H<sub>2</sub>/Ar and 2% O<sub>2</sub>/Ar were alternately introduced.

### 2.3. Catalytic activity measurements

Hg<sup>0</sup> oxidation activities over as-prepared catalysts were evaluated

with a fixed-bed reaction system as reported in our previous studies [29]. The catalyst dosage was 0.30 g for each test. The catalyst was placed in a borosilicate reactor with an inner diameter of 10 mm. The reactor was placed at the temperature of 200 °C, because the preliminary experiments found that ceria based catalysts presented optimal catalytic activity at this temperature. Compressed gas cylinders were used to provide the flue gas components except for water vapor (H<sub>2</sub>O), the flow rates of which were precisely controlled by mass flow controllers to be 1 L min<sup>-1</sup>. A stable gas-phase Hg<sup>0</sup> concentration ( $\sim 75 \mu\text{g m}^{-3}$ ) was provided by a Hg<sup>0</sup> permeation device (VICI Metronics) by heating the permeation tube to an unchanged temperature. Hg<sup>0</sup> concentrations at the reactor inlet ([Hg<sup>0</sup>]<sub>inlet</sub>) and outlet ([Hg<sup>0</sup>]<sub>outlet</sub>) were measured by an online mercury analyzer (Mercury Instruments Inc. VM3000).

The experiments could be separated into two sets. In Set I, Hg<sup>0</sup> remove performances of different ceria based catalysts were evaluated under N<sub>2</sub> or N<sub>2</sub> plus 4% O<sub>2</sub> atmospheres at 200 °C. The optimal Co-CeO<sub>2</sub> was adopted in the experiment of Set II to verify its application possibility in complicated coal combustion flue gas containing sulfur dioxide

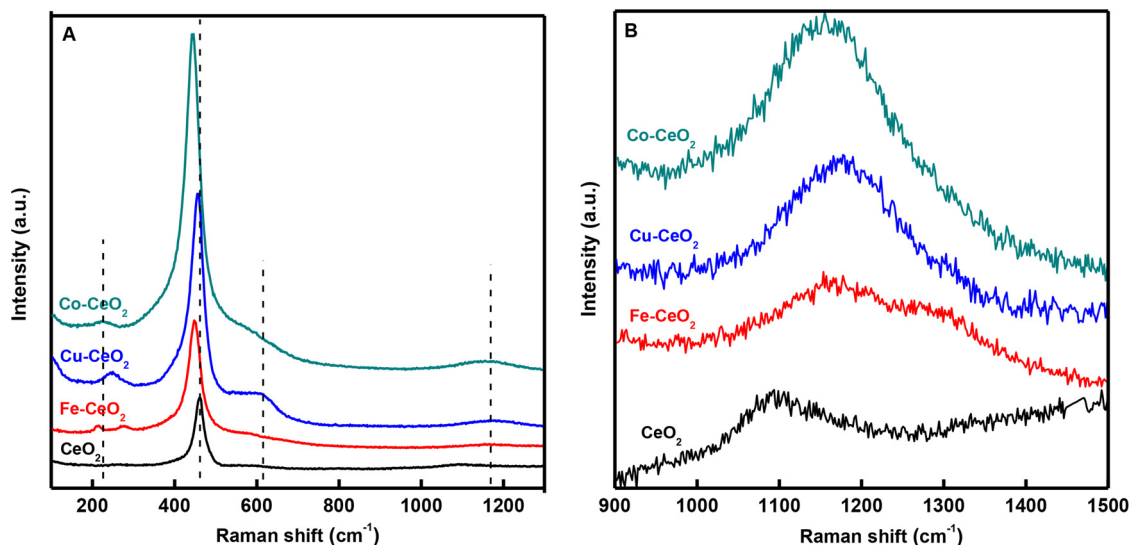


Fig. 4. Raman spectra (A) and the magnified view of the 2LO mode (B) of the pure  $\text{CeO}_2$ ,  $\text{Fe-CeO}_2$ ,  $\text{Cu-CeO}_2$ , and  $\text{Co-CeO}_2$ .

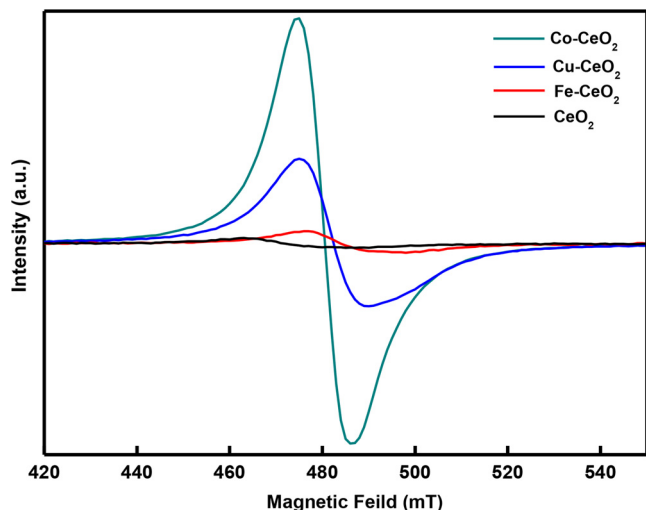


Fig. 5. EPR spectra of the pure  $\text{CeO}_2$ ,  $\text{Fe-CeO}_2$ ,  $\text{Cu-CeO}_2$ , and  $\text{Co-CeO}_2$ .

( $\text{SO}_2$ ) and  $\text{H}_2\text{O}$ . The  $[\text{Hg}^0]_{\text{inlet}}$  and  $[\text{Hg}^0]_{\text{outlet}}$  were recorded after the concentration variations were below 5% for 30 min. The  $\text{Hg}^0$  oxidation efficiency ( $E_{\text{oxi}}$ ) was calculated by Eq. (1):

$$E_{\text{oxi}} = ([\text{Hg}^0]_{\text{inlet}} - [\text{Hg}^0]_{\text{outlet}}) / [\text{Hg}^0]_{\text{inlet}} \times 100\% \quad (1)$$

### 3. Results

#### 3.1. Morphological and structural

As shown in Fig. 1, pure  $\text{CeO}_2$  presented as irregular agglomerates with a typical grain size about 100 nm. A lattice fringe with interplanar spacings of 0.31 nm could be observed in Fig. 1C1, suggesting the pure  $\text{CeO}_2$  selectively exposed (111) planes, as presented in Fig. 1D1. The  $\text{Fe-CeO}_2$  exhibited well-defined nanorods structure with lengths and diameters to be 450 nm and 250 nm, respectively. The HRTEM image of the  $\text{Fe-CeO}_2$  (Fig. 1C2) showed two interplanar spacings of 0.31 nm and 0.27 nm, which were attributed to (111) and (110) planes, indicating that  $\text{Fe-CeO}_2$  dominated by an octahedral shape (Fig. 1D2). For the  $\text{Cu-CeO}_2$  with nanorings structure, the inner and outer diameters were around 70 and 165 nm, respectively. The  $\text{Cu-CeO}_2$  sample showed a

clear (100) lattice fringe with interplanar spacings of 0.27 nm, which demonstrated that (100) was the dominant exposed plane of the  $\text{Cu-CeO}_2$  sample. The  $\text{Co-CeO}_2$  presented as uniform round nanoflakes with average diameter of 250 nm (Fig. 1B4). The corresponding HRTEM image suggests that (110) and (100) were the mainly exposed planes (Fig. 1C4, D4). Doping different metal cations into the  $\text{CeO}_2$  lattice resulted in ceria nanomaterials with different shape and size, and hence tuned the exposed planes, which is expected to affect the catalytic properties.

Table 1 shows the textural properties of as-prepared catalysts. All samples present a mesoporous structure with the average pore diameters in the range of 8.28–15.74 nm. The BET specific surface of pure  $\text{CeO}_2$  was  $90.71 \text{ m}^2 \text{ g}^{-1}$  and the pore volume was  $0.140 \text{ cm}^3 \text{ g}^{-1}$ . Compared with the pure  $\text{CeO}_2$ , the specific surface area and pore volume of  $\text{Cu-CeO}_2$  slightly increased, while that for the  $\text{Fe-CeO}_2$  and  $\text{Co-CeO}_2$  decreased obviously.

The XRD patterns of pure  $\text{CeO}_2$  and doped  $\text{CeO}_2$  samples have been displayed in Fig. 2. All the samples were well-crystallized, with all diffraction peaks well indexed to the fluorite cubic structures (JCPDS no. 34-0394). No diffraction peaks associated with doping-metal oxides phase were observed. This was due to the homogeneous distribution of doping ions in the framework of  $\text{CeO}_2$ , which was further confirmed by the EDS elemental mapping shown in Fig. 3. The ICP-AES analysis (Table 1) shows that Fe, Cu and Co contents of the samples were close to the those reported in the literature, which subsequently confirmed that the metals were actually doped into the ceria structure [14,30,31]. As shown in Table 1, the doped samples have smaller crystallite size than the pure  $\text{CeO}_2$ . This result suggested that the dopant introduces a lattice strain, which indicated the lattice distortion and lattice defects in the doped samples [32,33]. A slight shift in the {111} peak toward higher angles (Fig. 2B) and a decrease in lattice parameters (Table 1) on the  $\text{Fe-CeO}_2$  and  $\text{Co-CeO}_2$  indicate a contraction of the ceria lattice upon substitution of Ce with Fe and Co [34]. The lattice contraction was also confirmed by the decrease in crystallite size of  $\text{Fe-CeO}_2$  and  $\text{Co-CeO}_2$  [35]. In contrast, the {111} peak for  $\text{Cu-CeO}_2$  shifted toward smaller angle, indicating an expansion of the ceria lattice [36], which was due to the decrease in the cation valence state [33]. As mentioned above, the  $\text{Fe}^{3+}$ ,  $\text{Cu}^{2+}$  and  $\text{Co}^{2+}$  were successfully introduced into the  $\text{CeO}_2$  lattice, which would induce the lattice distortion and oxygen vacancy defects.

As presented in Fig. 4 a strong peak at around  $460 \text{ cm}^{-1}$  corresponds to the  $\text{F}_{2g}$  active mode of the  $\text{CeO}_2$  fluorite structure was observed in all prepared samples [34]. However, this band slightly red-

shifted with the substitution of Fe, Cu and Co into the  $\text{CeO}_2$  lattice. This is associated with the lattice distortion, in agreement with the XRD results [33,37]. The band at  $600\text{ cm}^{-1}$  was assigned to oxygen vacancies, which was probably caused by the existence of  $\text{Ce}^{3+}$  and the small size effect [38,39]. The small size effect would lead to defects and was confirmed by the smaller crystallite size of doped samples (shown

in Table 1). For the doped samples, the  $\text{F}_{2g}$  band became broader, originating from the increasing of the oxygen vacancies [40]. The maximum half width values of the  $\text{F}_{2g}$  peaks were in the sequence of  $\text{Co-CeO}_2 > \text{Cu-CeO}_2 > \text{Fe-CeO}_2 > \text{pure CeO}_2$ . This suggests that introducing metal cations promoted the formation of oxygen vacancies, and  $\text{Co-CeO}_2$  had the highest oxygen vacancies concentration. Raman peaks

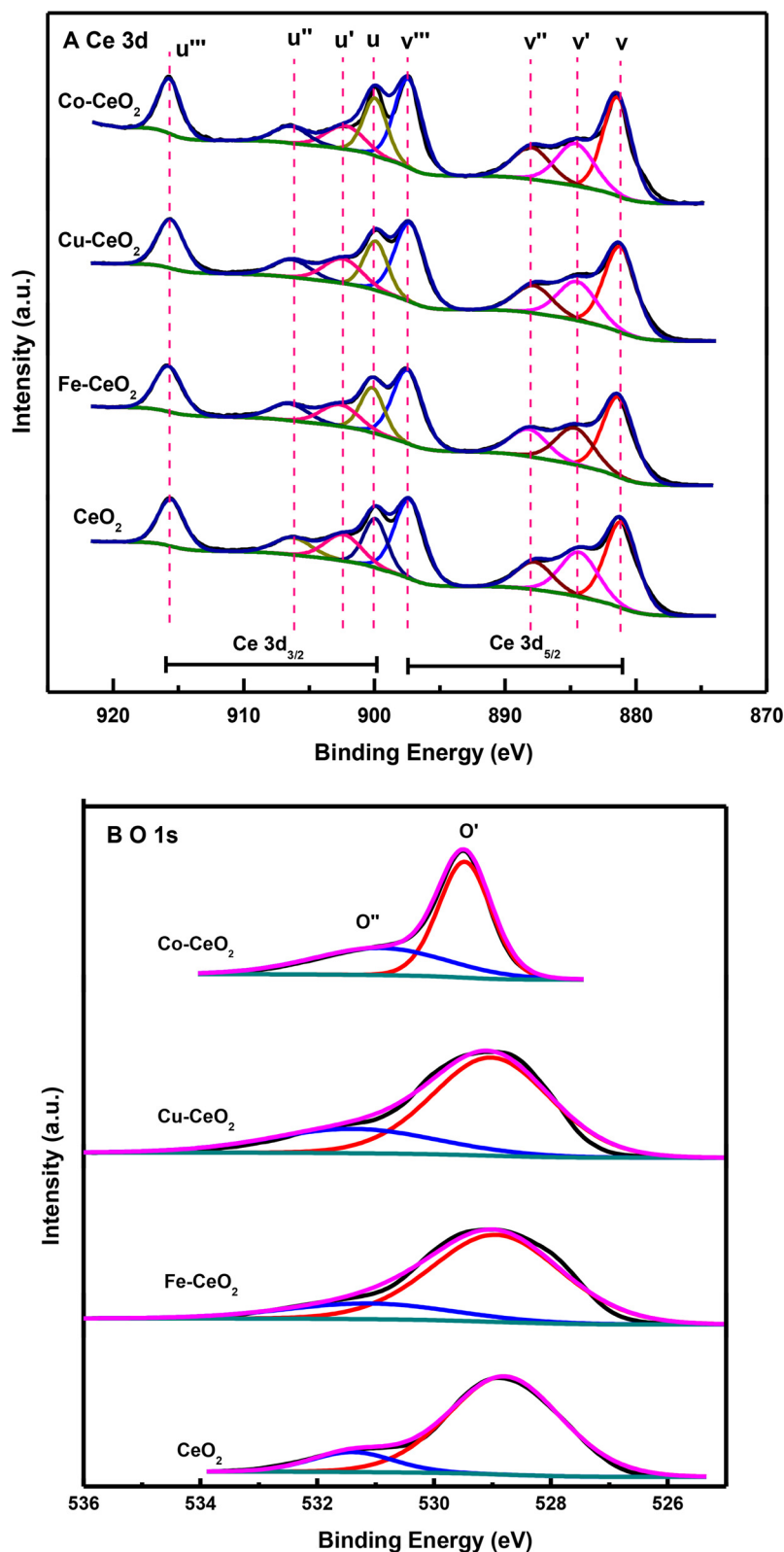


Fig. 6. XPS spectra of (A) Ce 3d, (B) O 1s for different catalysts, and (C) Co 2p for  $\text{Co-CeO}_2$ .

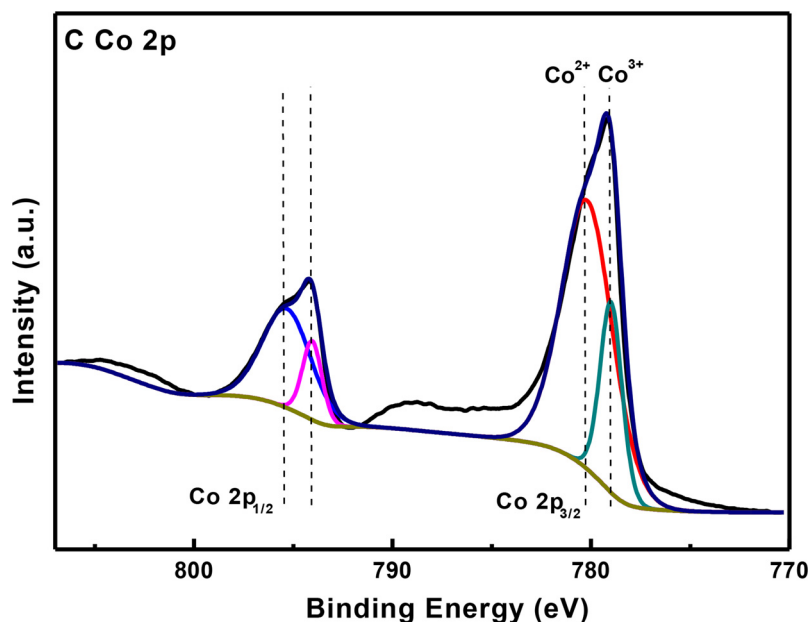


Fig. 6. (continued)

**Table 2**

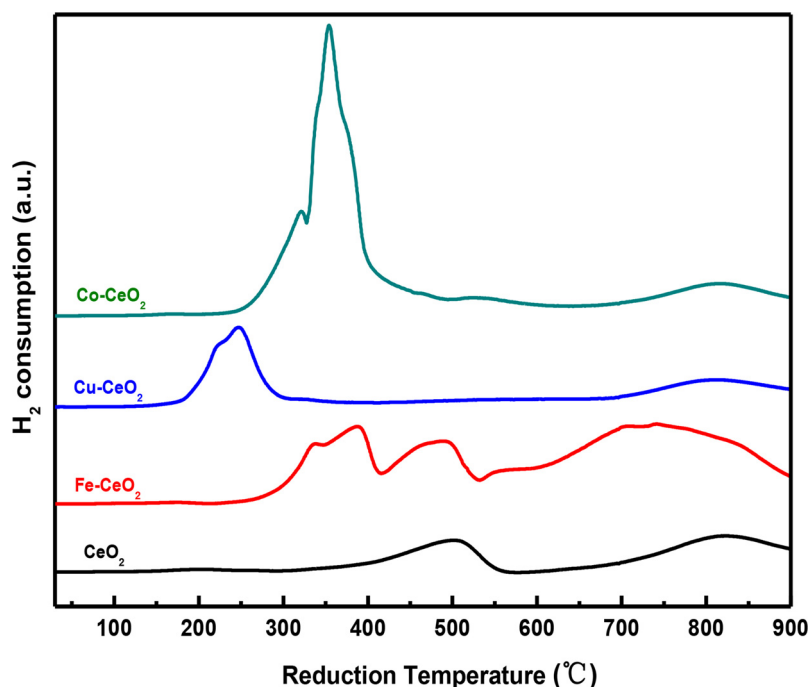
XPS analysis of the surface compositions for the samples.

Sample	Ce <sup>3+</sup> / (Ce <sup>3+</sup> + Ce <sup>4+</sup> ) (%)	Surface Atomic Ratio				O <sub>ads</sub> /(O <sub>latt</sub> + O <sub>ads</sub> ) (%)
		Ce (at%)	M (at%)	O (at%)	O/(Ce + M) (%)	
Pure CeO <sub>2</sub>	20.00	31.72	–	68.28	2.15	13.04
Fe-CeO <sub>2</sub>	20.01	20.60	12.93	66.47	1.98	18.70
Cu-CeO <sub>2</sub>	20.50	28.81	3.07	68.12	2.14	25.92
Co-CeO <sub>2</sub>	21.05	11.21	20.10	68.69	2.26	40.85

M represents Fe, Cu or Co.

around 250 cm<sup>-1</sup> and 1170 cm<sup>-1</sup> were attributed to a transverse acoustic mode and second-order longitudinal optical (2LO) mode in the ceria lattice [41]. The 2LO mode is related with the O–O stretching vibration mode of surface adsorbed superoxide species (O<sub>2</sub><sup>-</sup>). Therefore, the significant increase of 2LO mode clearly suggests more adsorbed oxygen trapped on the surface of Co-CeO<sub>2</sub> [42].

The EPR spectra of the pure CeO<sub>2</sub> and doped samples are illustrated in Fig. 5. All samples appeared an EPR signal when g-value was around 2.004, which was originated from the unpaired electrons trapping at oxygen vacancies [43,44]. The oxygen vacancy concentrations corresponding to the signal intensity followed by the order of Co-CeO<sub>2</sub>, Cu-CeO<sub>2</sub>, Fe-CeO<sub>2</sub> and finally CeO<sub>2</sub>. This is agreeing well with the tendency obtained from the Raman spectra. It should be noted that the g-values of doped materials were slightly different from that of pure CeO<sub>2</sub>, which

Fig. 7. H<sub>2</sub>-TPR curves of pure CeO<sub>2</sub>, Fe-CeO<sub>2</sub>, Cu-CeO<sub>2</sub>, and Co-CeO<sub>2</sub>.

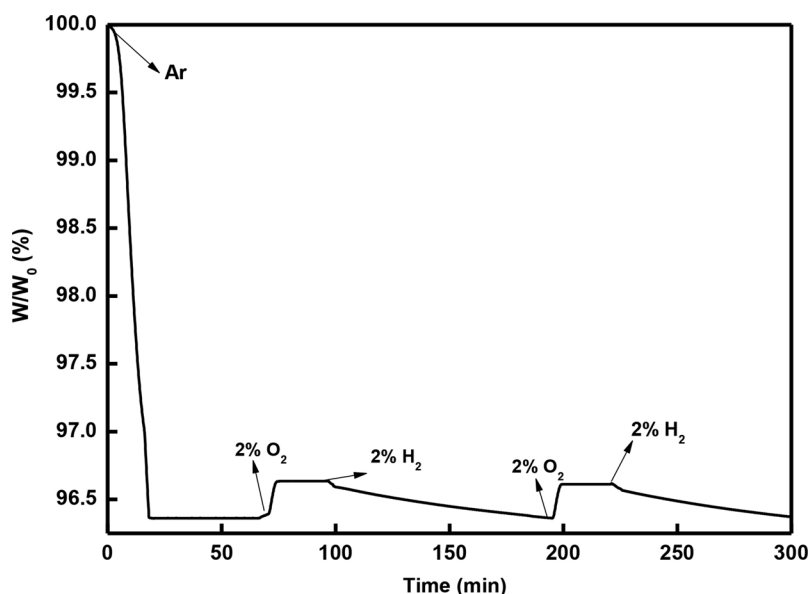


Fig. 8. Oxygen releasing and recovering over the Co-CeO<sub>2</sub> at 200 °C.

was probably due to the changes in the electron coupling of the surface superoxide-like species [45,46]. This further implies that the introduction of doping ions gave rise to more oxygen vacancies, thus would generate more surface active oxygen.

### 3.2. Oxygen storage capacity

The surface elemental composition was obtained by the analysis of XPS spectra, especially the surface oxygen content. As shown in Fig. 6A, the peaks of u''', u'', u and v'', v characterized the Ce<sup>4+</sup> 3d<sub>3/2</sub> and Ce<sup>4+</sup> 3d<sub>5/2</sub> due to the spin-orbit splitting. On the other hand, u' and v' belonged to Ce<sup>3+</sup> 3d<sub>3/2</sub> and Ce<sup>3+</sup> 3d<sub>5/2</sub> peaks, respectively [47]. For all samples, cerium mainly existed in a +4-oxidation state. The surface molar ratio of Ce<sup>3+</sup>/(Ce<sup>3+</sup> + Ce<sup>4+</sup>) slightly differed for all samples, with Co-CeO<sub>2</sub> exhibited the largest Ce<sup>3+</sup>/(Ce<sup>3+</sup> + Ce<sup>4+</sup>) ratio of 21.05%.

Broad peaks on the O 1s XPS spectra suggesting the existence of different types of surface oxygen species on all these CeO<sub>2</sub> based catalysts (Fig. 6B). The main peaks at 528.8–529.2 eV were the characteristic peaks of the surface lattice oxygen (O<sub>latt</sub>) bonding to metal cations, whereas the peaks located at 530.9–531.3 eV were considered as the surface adsorbed oxygen originated from the oxygen defects (O<sub>ads</sub>) [3,48]. As listed in Table 2, the O<sub>ads</sub>/(O<sub>latt</sub> + O<sub>ads</sub>) ratios for doped CeO<sub>2</sub> were higher than that for pure CeO<sub>2</sub>. The Co-CeO<sub>2</sub> exhibited the highest O<sub>ads</sub>/(O<sub>latt</sub> + O<sub>ads</sub>) ratio of 40.85%, much higher than that for Cu and Fe doped samples, and even up to three times of that for the pure CeO<sub>2</sub>.

The Co 2p XPS spectrum (Fig. 6C) for Co-CeO<sub>2</sub> displays two intense peaks of Co 2p<sub>3/2</sub> and Co 2p<sub>1/2</sub> with an energy gap of 15.2 eV [40], which indicates the existence of Co<sup>2+</sup> and Co<sup>3+</sup> on the Co-CeO<sub>2</sub> surface [49]. The 2p<sub>3/2</sub> spectrum fitted into two peaks corresponding to Co<sup>2+</sup> (the peak at 780.2 eV) and Co<sup>3+</sup> (the peak at 779.1 eV) indicates that Co<sup>2+</sup> was the main Co species [50]. The Co<sup>2+</sup>/Co<sup>3+</sup> molar ratio as high as 3.80 indicates larger amount of oxygen defects, which could compensate by O<sub>ads</sub> on the surface [49]. Thus, the high Co<sup>2+</sup> content on the surface of Co-CeO<sub>2</sub> would be one reason for the high O<sub>ads</sub>/(O<sub>latt</sub> + O<sub>ads</sub>) ratio of the catalyst.

H<sub>2</sub>-TPR was employed to analyze the reducibility of the materials. Two obvious characteristic reduction peaks could be seen in the H<sub>2</sub>-TPR profile of the pure CeO<sub>2</sub> (Fig. 7): the peak at 510 °C was resulted from the consumption of surface oxygen [51], while the spike locating at 820 °C was due to the bulk oxygen reduction [52]. Compared to the

pure ceria, the reduction peaks for all the doped ceria shifted to a lower temperature range, indicating that stored oxygen on the doped ceria was more reactive. This was probably due to the structural modifications by the substitution of Fe, Cu and Co into the CeO<sub>2</sub> lattice, which promoted the diffusion of the O<sup>2-</sup> within the lattice, and hence improved the oxygen mobility as well as accelerated the migration of bulk oxygen to replenish surface oxygen during the surface reduction by H<sub>2</sub> [53–55]. For the multiple reduction peaks around 300–550 °C in the profile of Fe-CeO<sub>2</sub>, it was probably caused by the reduction of Fe species appearing in the material surface, which has been reported previously [14,45]. Notably, the maximum hydrogen consumption was observed over the Co-CeO<sub>2</sub>, suggesting the Co-CeO<sub>2</sub> storing a large amount of oxygen vacancies and abundant oxygen on its surface, in line with the XPS results.

As the optimal temperature for Hg<sup>0</sup> remove over the CeO<sub>2</sub> based catalysts was about 200 °C [56,57], the OSC of the best Co-CeO<sub>2</sub> catalyst was measured using a TG method conducted at 200 °C. The introduction of 2% H<sub>2</sub>/Ar after the sample weight was stabilized resulted in a releasing of oxygen and a 0.3% decreasing of weight, which could be seen in Fig. 8. When the 2% O<sub>2</sub>/Ar gas was subsequently introduced, the Co-CeO<sub>2</sub> surface was quickly oxidized and the sample weight recovered back to the original level. The OSC value per surface area calculated from the weight loss during the oxygen releasing process was as high as 1.43 μmol O<sub>2</sub> m<sup>-2</sup>, which is much higher than the reported CeO<sub>2</sub> nanorods (0.80 μmol O<sub>2</sub> m<sup>-2</sup>) and the cubic CeO<sub>2</sub> (0.57 μmol O<sub>2</sub> m<sup>-2</sup>) at 200 °C [19,58]. According to the XPS results, the ratio of O<sub>ads</sub>/(O<sub>ads</sub> + O<sub>latt</sub>) were in the sequence of Co-CeO<sub>2</sub> > Cu-CeO<sub>2</sub> > Fe-CeO<sub>2</sub> > pure CeO<sub>2</sub>, which is agreeing well with the reduction peaks and hydrogen consumption tendency obtained from the H<sub>2</sub>-TPR results [59], revealing the increasing of oxygen vacancies and the abundant oxygen on the surface of the doped materials. TGA results show a superior OSC value for the Co-CeO<sub>2</sub> sample. Therefore, all these XPS, H<sub>2</sub>-TPR and TGA results confirm that the Co-CeO<sub>2</sub> has large OSC at the operating temperature for Hg<sup>0</sup> oxidation, and most of them are active chemisorbed oxygen.

### 3.3. Catalytic performance in Hg<sup>0</sup> oxidation

Hg<sup>0</sup> physical adsorption over metal oxides has been reported previously [60,61] and identified in our preliminary study to be negligible. Without the presence of gas phase oxygen, Mars-Maessen (M-M) mechanism mainly accounted for the Hg<sup>0</sup> oxidation with the surface stored



oxygen [7,62]. Fig. 9 shows  $\text{Hg}^0$  oxidation over the pure  $\text{CeO}_2$  and the doped  $\text{CeO}_2$  samples at 200 °C. Relatively small amounts of  $\text{Hg}^0$  were oxidized over the pure  $\text{CeO}_2$  and  $\text{Fe-CeO}_2$  under  $\text{N}_2$  atmosphere. The performance of  $\text{Cu-CeO}_2$  in  $\text{Hg}^0$  oxidation under  $\text{N}_2$  atmosphere was better than that over the pure  $\text{CeO}_2$  and  $\text{Fe-CeO}_2$ . However, without oxygen replenishment by gas phase  $\text{O}_2$ , the downstream  $\text{Hg}^0$  concentration climbed from 10.9 to  $16.5 \mu\text{g m}^{-3}$  in 6 min. Notably,  $\text{Co-CeO}_2$  exhibited superior  $\text{Hg}^0$  oxidation performance under  $\text{N}_2$  atmosphere. After passing through the  $\text{Co-CeO}_2$  catalyst,  $\text{Hg}^0$  concentration decreased from about 75.0 to less than  $2.0 \mu\text{g m}^{-3}$  during the entire experimental period. The  $\text{Hg}^0$  oxidation activity under  $\text{N}_2$  atmosphere of these four samples followed the sequence of  $\text{Co-CeO}_2 > \text{Cu-CeO}_2 > \text{Fe-CeO}_2 > \text{pure CeO}_2$ , which is very consistent with the surface storage capacity for chemisorbed oxygen. This phenomenon suggests that it was the chemisorbed oxygen played important role in oxidizing  $\text{Hg}^0$  without gas phase  $\text{O}_2$ . Gas phase  $\text{O}_2$  regenerated a part of consumed  $\text{O}_{\text{ads}}$ , which acted as the  $\text{Hg}^0$  oxidant. Therefore, the  $\text{Hg}^0$  oxidation efficiency of the pure  $\text{CeO}_2$ ,  $\text{Fe-CeO}_2$  and  $\text{Cu-CeO}_2$  increased with the introduction of gas phase  $\text{O}_2$ . It is also worth noting that the

BET surface area and pore volume of the catalysts play insignificant role in  $\text{Hg}^0$  catalytic oxidation, as  $\text{Co-CeO}_2$  had smaller surface and pore volume but presented the best catalytic activity. For the optimal  $\text{Co-CeO}_2$ , the XPS results of O 1s and Hg 4f of the  $\text{Co-CeO}_2$  after  $\text{Hg}^0$  removal experiment are given in Fig. 10. The consuming of surface chemisorbed oxygen during  $\text{Hg}^0$  oxidation process resulted in a decrease of the  $\text{O}_{\text{ads}}/(\text{O}_{\text{latt}} + \text{O}_{\text{ads}})$  ratio from 40.85% to 28.25%. The XPS spectrum of Hg 4f shows two peaks at 102.6 eV and 101.6 eV, indicating the appearance of  $\text{HgO}$  on the catalyst surface [5,63]. This suggests that  $\text{Hg}^0$  oxidation occurred through the M-M mechanism, in which the adsorbed  $\text{Hg}^0$  was oxidized by active chemisorbed oxygen originated from oxygen vacancy defects to form  $\text{HgO}$ .

Moreover, the  $\text{Hg}^0$  oxidation efficiency of  $\text{Co-CeO}_2$  catalyst under simulated flue gas (SFG) has been investigated. The SFG components consisted of 4%  $\text{O}_2$ , 10 ppm  $\text{HCl}$ , 300 ppm  $\text{NO}$ , 500 ppm  $\text{SO}_2$ , 8%  $\text{H}_2\text{O}$  and  $75 \mu\text{g m}^{-3}$   $\text{Hg}^0$ , balanced in  $\text{N}_2$ , which represented the typical low-rank coal combustion flue gas. The flue gas components might lead to inconclusive influences on  $\text{Hg}^0$  oxidation over different catalysts. As shown in Fig. 11, the  $\text{Hg}^0$  oxidation efficiency in a SFG environment

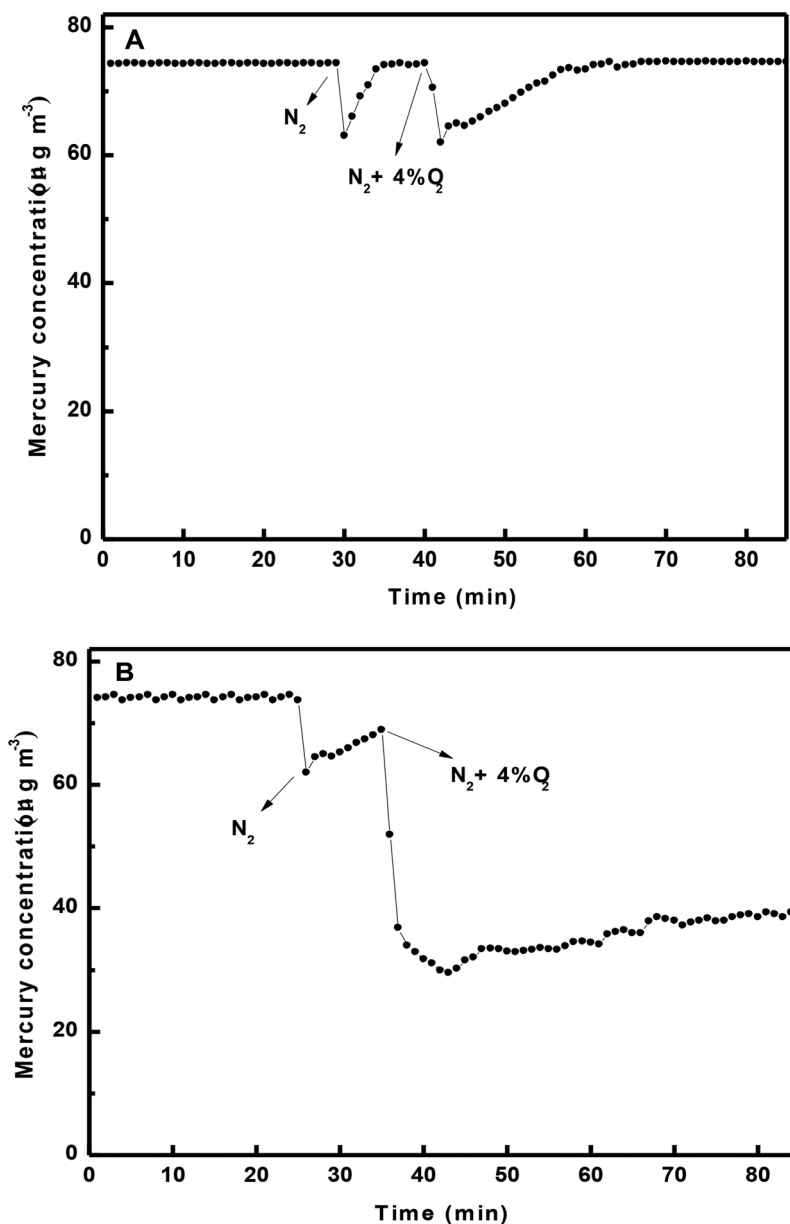


Fig. 9.  $\text{Hg}^0$  oxidation over the pure  $\text{CeO}_2$  (A),  $\text{Fe-CeO}_2$  (B),  $\text{Cu-CeO}_2$  (C), and  $\text{Co-CeO}_2$  (D) at 200 °C.

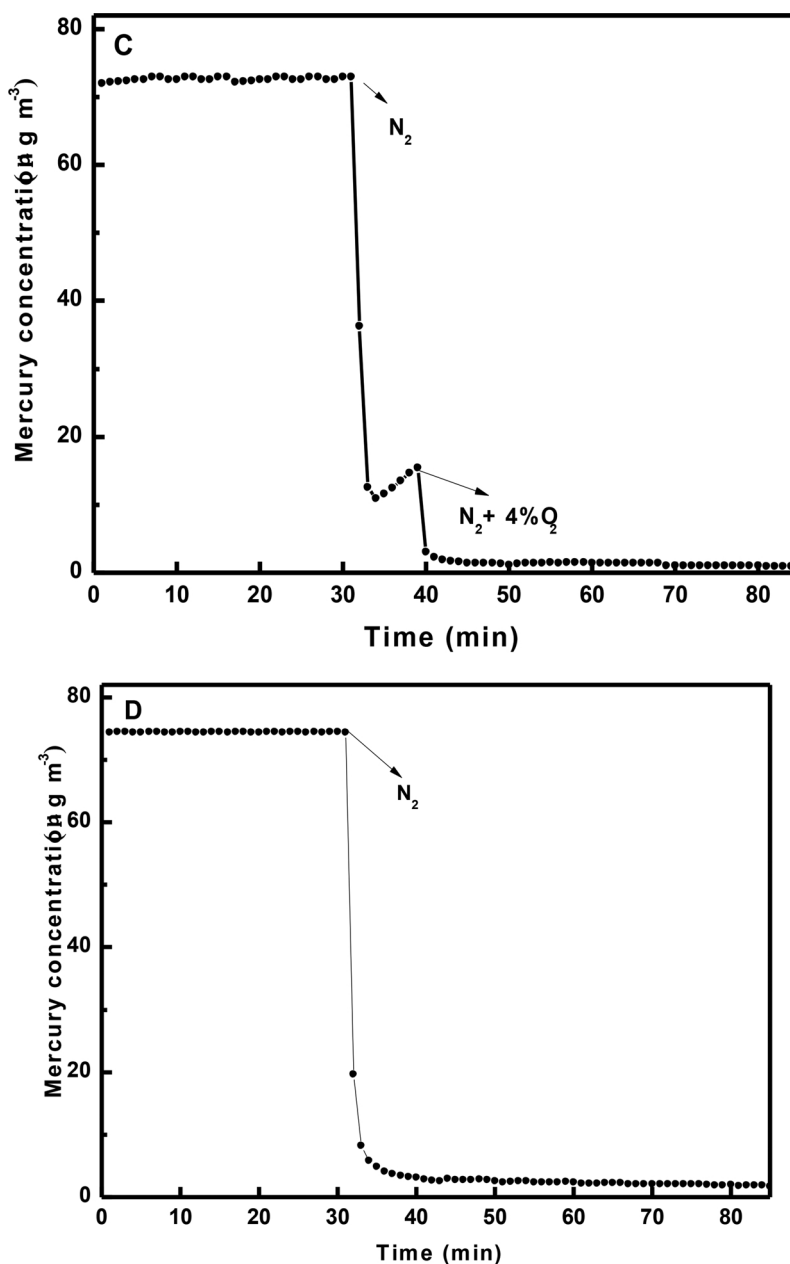


Fig. 9. (continued)

was achieved to 91.8% when a gas hourly space velocity (GHSV) was as high as  $160,000 \text{ h}^{-1}$ . It should be noted that the SFG represents the flue gases of the low-rank coal combustion, which was widely identified to be adverse for  $Hg^0$  oxidation. The flue gases from high-rank coal combustion contained a higher HCl concentration, meanwhile, the lower GHSV could further facilitate  $Hg^0$  oxidation. Thus, Co-CeO<sub>2</sub> catalyst is promising in future application  $Hg^0$  oxidation in coal-fired power plants.

Fig. 11 presents the  $Hg^0$  oxidation over Co-CeO<sub>2</sub> in the presence of SO<sub>2</sub> and H<sub>2</sub>O. Fig. 11A shows that increasing the SO<sub>2</sub> concentration caused a slight inhibition in  $Hg^0$  oxidation. However, above 80%  $Hg^0$  oxidation was still obtained when the SO<sub>2</sub> concentration was as high as 1500 ppm. Water vapor also slightly inhibited  $Hg^0$  oxidation. It is worth noting  $Hg^0$  oxidation efficiency higher than 82% was obtained even the H<sub>2</sub>O content was up to 25%. Moreover, lower GHSV for actual coal combustion flue gas would at least partly relieve the inhibitive effect of SO<sub>2</sub> and H<sub>2</sub>O, and more  $Hg^0$  oxidation would be achieved. Therefore, these results suggest that the Co-CeO<sub>2</sub> catalyst has superior SO<sub>2</sub> and

H<sub>2</sub>O resistance during the  $Hg^0$  oxidation process, indicating the potential to be an applicable catalyst for  $Hg^0$  oxidation in a real-world condition.

#### 4. Discussions

The introduction of Fe, Cu, and Co into the CeO<sub>2</sub> lattice caused lattice distortion, and hence resulted in CeO<sub>2</sub> based catalysts with different shape and size. After doping metal cations into the CeO<sub>2</sub> lattice, the irregular CeO<sub>2</sub> agglomerates transformed to nanorods, nanorings, and nanoflakes for Fe-CeO<sub>2</sub>, Cu-CeO<sub>2</sub>, and Co-CeO<sub>2</sub>, respectively. More (110) and (100) planes were exposed on the flake-shaped Co-CeO<sub>2</sub>. As the oxygen vacancy formation energies on (110) and (100) planes are lower than that on (111) plane, more oxygen vacancy defects were formed on the Co-CeO<sub>2</sub>, which was confirmed by the Raman and EPR spectra. The high Co<sup>2+</sup>/Co<sup>3+</sup> molar ratio of 3.8 and the redox couples (Co<sup>2+</sup>/Co<sup>3+</sup> and Ce<sup>3+</sup>/Ce<sup>4+</sup>) [64] further verified the existing of abundant oxygen vacancy defects on the Co-CeO<sub>2</sub>. For the

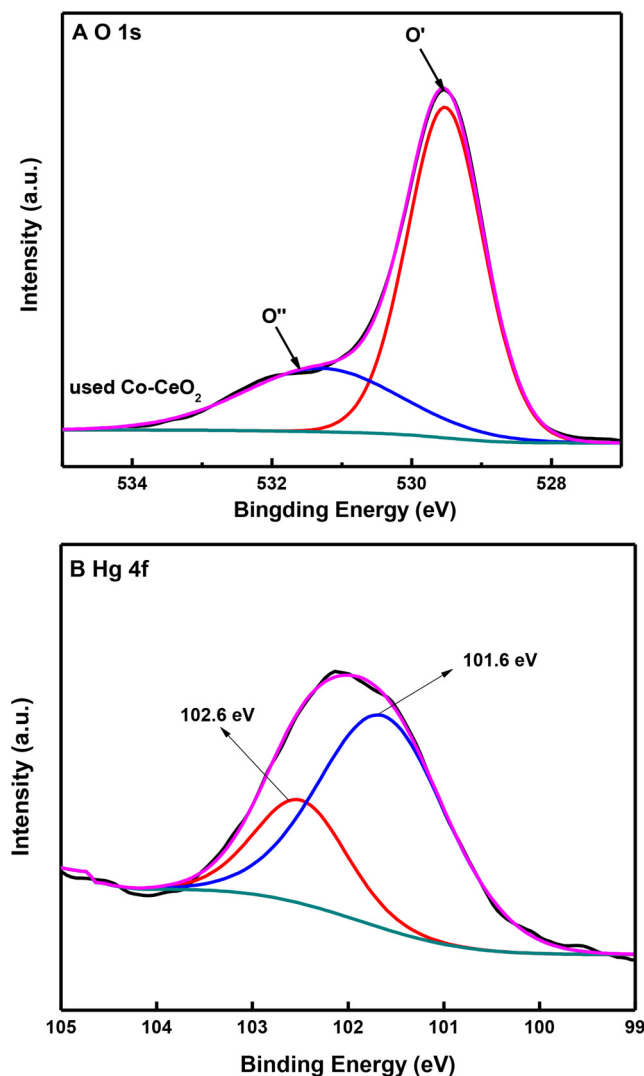


Fig. 10. XPS spectra of (A) O 1s, (B) Hg 4f for the Co-CeO<sub>2</sub> after Hg<sup>0</sup> oxidation experiment.

compensation of oxygen vacancy surface oxygen is needed. Therefore, plentiful active oxygen was generated on the Co-CeO<sub>2</sub> surface. The  $O_{\text{ads}}/(O_{\text{latt}} + O_{\text{ads}})$  ratio for the Co-CeO<sub>2</sub> was up to 40.85%, which is three times larger than that for the pure CeO<sub>2</sub>. Moreover, the structural modification by the substitution of Co into the ceria lattice would probably promote the O<sup>2-</sup> diffusion within the lattice to replenish surface oxygen consumed during the surface reduction by H<sub>2</sub>. Therefore, an OSC value of 1.43  $\mu\text{mol O}_2 \text{ m}^{-2}$  for the Co-CeO<sub>2</sub> was obtained through measuring the weight loss during an oxygen releasing process under 2% H<sub>2</sub>/Ar atmosphere. Compare to reported CeO<sub>2</sub> nanorods and cubic CeO<sub>2</sub>, the OSC value of Co-CeO<sub>2</sub> nanoflakes is much higher, demonstrating that it is technically feasible to adjust OSC of CeO<sub>2</sub> based catalysts through incorporating foreign metal ions.

With the high OSC, Co-CeO<sub>2</sub> exhibited superior Hg<sup>0</sup> oxidation performance even without O<sub>2</sub>. More than 98% of Hg<sup>0</sup> was oxidized during the entire experimental period. As stated above, Hg<sup>0</sup> oxidation over the Co-CeO<sub>2</sub> occurred through the M-M mechanism, in which weakly adsorbed Hg<sup>0</sup> reacted with chemisorbed surface oxygen to form HgO. Abundant chemisorbed surface oxygen on the Co-CeO<sub>2</sub> played pivotal role in Hg<sup>0</sup> oxidation when gas phase O<sub>2</sub> was scarce, and could be replenished by gaseous O<sub>2</sub>. Even though H<sub>2</sub>O and SO<sub>2</sub> slightly limited Hg<sup>0</sup> oxidation, active chlorine species generated from the reactions between the trace amount HCl in flue gas and chemisorbed surface oxygen [8] probably guaranteed an efficient Hg<sup>0</sup> oxidation. Therefore, Hg<sup>0</sup>

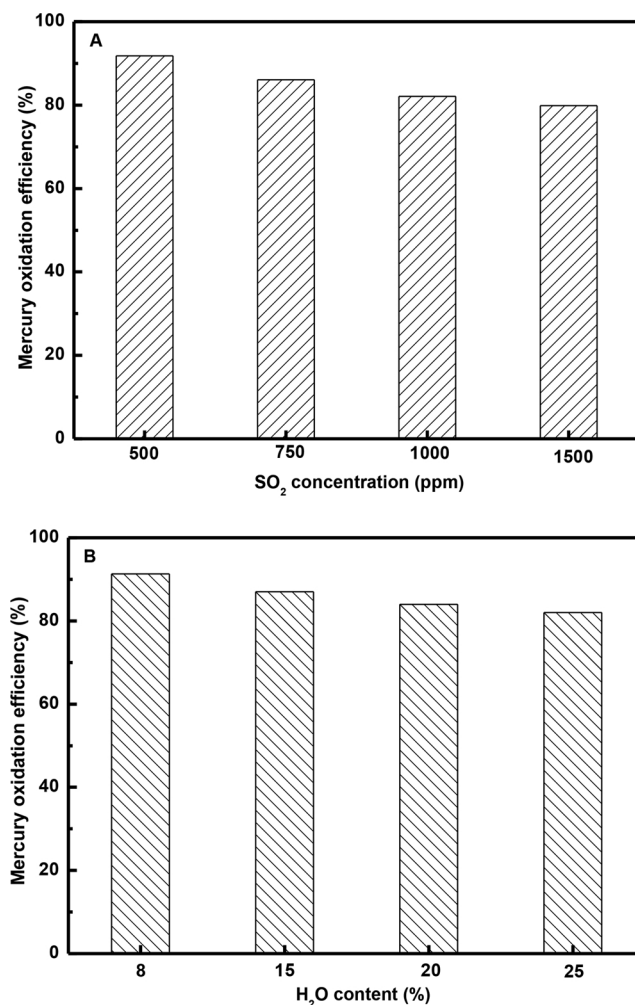


Fig. 11. Effect of SO<sub>2</sub> (A) and H<sub>2</sub>O (B) on Hg<sup>0</sup> oxidation over the Co-CeO<sub>2</sub>.

oxidation efficiency higher than 80% was still achieved in SFG environment even the SO<sub>2</sub> and H<sub>2</sub>O contents were as high as 1500 ppm and 25%, respectively. It should be noted the adverse conditions were applied like the low-rank burning flue gas components, which means low HCl concentration, and far higher GHSV compared with a real condition. Previous report found that more HCl was contained in high-rank coal burning flue gases, and the lower GHSV could further facilitate Hg<sup>0</sup> conversion [65]. In addition, the Co-CeO<sub>2</sub> would probably perform even better in the Hg<sup>0</sup> oxidation performance by optimizing the Co-CeO<sub>2</sub> composition in the future. Therefore, the applications of Co-CeO<sub>2</sub> catalyst capable of efficient oxidation of Hg<sup>0</sup> to Hg<sup>2+</sup> would be beneficial to economically control mercury emission from power plants.

## 5. Conclusions

Addition Co into the CeO<sub>2</sub> lattice changed the irregular CeO<sub>2</sub> agglomerates into Co-CeO<sub>2</sub> nanoflakes due to the induced lattice contraction. The mainly exposed (110) and (100) planes on the Co-CeO<sub>2</sub> nanoflakes surface lowered the oxygen vacancy formation energy, and hence resulted in plentiful oxygen vacancy defects, which further led to abundant surface chemisorbed oxygen. With the aid of abundant surface chemisorbed oxygen, the Co-CeO<sub>2</sub> performed very well in Hg<sup>0</sup> oxidation in the absence of gaseous O<sub>2</sub>. The Hg<sup>0</sup> oxidation was proposed to through the M-M mechanism, i.e., the adsorbed Hg<sup>0</sup> reacted with active chemisorbed oxygen originated from oxygen vacancy defects to form HgO. Even the GHSV was extremely high, more than 90% Hg<sup>0</sup> was oxidized under a simulated low-rank coal burning flue gas

atmosphere, suggesting that the Co-CeO<sub>2</sub> was highly efficient in Hg<sup>0</sup> oxidation. The negligible prohibitive effects of SO<sub>2</sub> and H<sub>2</sub>O warrant it to be a promising Hg<sup>0</sup> oxidation catalyst that could be applied in actual coal combustion flue gas.

## Acknowledgements

This work was supported by the National Natural Science Foundation of China (51774338, 51776227), Major science and technology projects in Gansu province (1602FKDC007) and Key Project of Chinese National Research Programs (2016YFC0403003).

## References

- [1] K. Schofield, *Combust. Flame* 159 (2012) 1741–1747.
- [2] H. Li, S. Wu, C. Wu, J. Wang, L. Li, K. Shih, *Environ. Sci. Technol.* 49 (2015) 7373–7379.
- [3] L. Zhao, C. Li, S. Li, Y. Wang, J. Zhang, T. Wang, G. Zeng, *Appl. Catal. B-Environ.* 198 (2016) 420–430.
- [4] L. Zhao, C. Li, Y. Wang, H. Wu, L. Gao, J. Zhang, G. Zeng, *Catal. Sci. Technol.* 6 (2016) 6076–6086.
- [5] H. Xu, Z. Qu, C. Zong, F. Quan, J. Mei, N. Yan, *Appl. Catal. B: Environ.* 186 (2016) 30–40.
- [6] Z. Liu, V. Sriram, J. Lee, *Appl. Catal. B-Environ.* 207 (2017) 143–152.
- [7] A.A. Presto, E.J. Granite, *Environ. Sci. Technol.* 40 (2006) 5601–5609.
- [8] H. Li, C. Wu, Y. Li, J. Zhang, *Environ. Sci. Technol.* 45 (2011) 7394–7400.
- [9] Z. Liu, D. Wang, B. Peng, L. Chai, H. Liu, S. Yang, B. Yang, K. Xiang, C. Liu, *Environ. Sci. Pollut. Res.* 24 (2017) 22494–22502.
- [10] B. Dranga, L. Lazar, H. Koeser, *Catalysts* 2 (2012) 139–170.
- [11] Y. Gao, Z. Zhang, J. Wu, L. Duan, A. Umar, L. Sun, Z. Guo, Q. Wang, *Environ. Sci. Technol.* 47 (2013) 10813–10823.
- [12] L. Ling, M. Fan, B. Wang, R. Zhang, *Energy Environ. Sci.* 8 (2015) 3109–3133.
- [13] Y. Cao, B. Chen, J. Wu, H. Cui, J. Smith, C. Chen, P. Chu, W. Pan, *Energy Fuel* 21 (2007) 145–156.
- [14] T.R. Sahoo, M. Armandi, R. Arletti, M. Piumetti, S. Bensaid, M. Manzoli, S.R. Panda, B. Bonelli, *Appl. Catal. B-Environ.* 211 (2017) 31–45.
- [15] C. He, B. Shen, J. Chen, J. Cai, *Environ. Sci. Technol.* 48 (2014) 7891–7898.
- [16] Q. Wan, Q. Yao, L. Duan, X. Li, L. Zhang, J. Hao, *Environ. Sci. Technol.* 52 (2018) 2981–2987.
- [17] J. Zhou, W. Hou, P. Qi, X. Gao, Z. Luo, K. Cen, *Environ. Sci. Technol.* 47 (2013) 10056–10062.
- [18] Z. Qiao, Z. Wu, S. Dai, *ChemSusChem* 6 (2013) 1821–1833.
- [19] Y. Ishikawa, M. Takeda, S. Tsukimoto, K.S. Nakayama, N. Asao, *Adv. Mater.* 28 (2016) 1467–1471.
- [20] W. Huang, Y. Gao, *Catal. Sci. Technol.* 4 (2014) 3772–3784.
- [21] D.R. Mullins, *Surf. Sci. Rep.* 70 (2015) 42–85.
- [22] M.V. Ganduglia-Pirovano, A. Hofmann, J. Sauer, *Surf. Sci. Rep.* 62 (2007) 219–270.
- [23] W. Liu, X. Liu, L. Feng, J. Guo, A. Xie, S. Wang, J. Zhang, Y. Yang, *Nanoscale* 6 (2014) 10693–10700.
- [24] X. Guo, C. Mao, J. Zhang, J. Huang, W. Wang, Y. Deng, Y. Wang, Y. Cao, W. Huang, S. Yu, *Small* 8 (2012) 1515–1520.
- [25] D. Mukherjee, B.G. Rao, B.M. Reddy, *Appl. Catal. B-Environ.* 197 (2016) 105–115.
- [26] F. Wang, W. Li, X. Feng, D. Liu, Y. Zhang, *Chem. Sci.* 7 (2016) 1867–1873.
- [27] S.M. Vickers, R. Gholami, K.J. Smith, M.J. MacLachlan, *ACS Appl. Mater. Interfaces* 7 (2015) 11460–11466.
- [28] A.B. Kehoe, D.O. Scanlon, G.W. Watson, *Chem. Mater.* 23 (2011) 4464–4468.
- [29] S. Jiang, X. Liu, H. Li, J. Wang, Z. Yang, H. Peng, K. Shih, *Fuel* 215 (2018) 232–238.
- [30] P. Venkataswamy, D. Jampaiah, C.U. Aniz, B.M. Reddy, *J. Chem. Sci.* 127 (2015) 1347–1360.
- [31] R. Si, J. Raitano, N. Yi, L. Zhang, S. Chan, M. Flytzani-Stephanopoulos, *Catal. Today* 180 (2012) 68–80.
- [32] Z. Shi, P. Yang, F. Tao, R. Zhou, *Chem. Eng. J.* 295 (2016) 99–108.
- [33] A.V. Thorat, T. Ghoshal, P. Carolan, J.D. Holmes, M.A. Morris, *J. Phys. Chem. C* 118 (2014) 10700–10710.
- [34] C. Artini, M. Pani, M.M. Carnasciali, M.T. Buscaglia, J.R. Plaisier, G.A. Costa, *Inorg. Chem.* 54 (2015) 4126–4137.
- [35] L. Chen, P. Fleming, V. Morris, J.D. Holmes, M.A. Morris, *J. Phys. Chem. C* 114 (2010) 12909–12919.
- [36] R. Farra, M. Garcia-Melchor, M. Eichelbaum, M. Hashagen, W. Frandsen, J. Allan, F. Girgsdies, L. Szentmiklosi, N. Lopez, D. Teschner, *ACS Catal.* 3 (2013) 2256–2268.
- [37] W. Deng, Q. Dai, Y. Lao, B. Shi, X. Wang, *Appl. Catal. B-Environ.* 181 (2016) 848–861.
- [38] N. Yang, Y. Shi, S. Schweiger, E. Strelcov, A. Belianinov, V. Foglietti, P. Orgiani, G. Balestrino, S.V. Kalinin, J.L.M. Rupp, C. Aruta, *ACS Appl. Mater. Interfaces* 8 (2016) 14613–14621.
- [39] G. Niu, E. Hildebrandt, M.A. Schubert, F. Boscherini, M.H. Zoellner, L. Alff, D. Walczyk, P. Zaumseil, I. Costina, H. Wilkens, T. Schroeder, *ACS Appl. Mater. Interfaces* 6 (2014) 17496–17505.
- [40] J. Mei, Y. Ke, Z. Yu, X. Hu, Z. Qu, N. Yan, *Chem. Eng. J.* 320 (2017) 124–134.
- [41] T. Taniguchi, T. Watanabe, N. Sugiyama, A.K. Subramani, H. Wagata, N. Matsushita, M. Yoshimura, *J. Phys. Chem. C* 113 (2009) 19789–19793.
- [42] B. Choudhury, P. Chetri, A. Choudhury, *RSC Adv.* 4 (2014) 4663–4671.
- [43] Y. Zhang, Z. Li, L. Zhang, L. Pan, X. Zhang, L. Wang, Fazal-e-Aleem, J. Zou, *Appl. Catal. B-Environ.* 224 (2018) 101–108.
- [44] F. Lei, Y. Sun, K. Liu, S. Gao, L. Liang, B. Pan, Y. Xie, *J. Am. Chem. Soc.* 136 (2014) 6826–6829.
- [45] W. Wang, Q. Zhu, Q. Dai, X. Wang, *Chem. Eng. J.* 307 (2017) 1037–1046.
- [46] W. Wang, Q. Zhu, F. Qin, Q. Dai, X. Wang, *Chem. Eng. J.* 333 (2018) 226–239.
- [47] C. Shan, Y. Xu, M. Hua, M. Gu, Z. Yang, P. Wang, Z. Lu, W. Zhang, B. Pan, *Chem. Eng. J.* 338 (2018) 261–270.
- [48] M. Kurnatowska, W. Mista, P. Mazur, L. Kepinski, *Appl. Catal. B-Environ.* 148 (2014) 123–135.
- [49] J. Gonzalez-Prior, R. Lopez-Fonseca, J.I. Gutierrez-Ortiz, B. de Rivas, *Appl. Catal. B-Environ.* 199 (2016) 384–393.
- [50] J. Zhou, J. Zhang, A.U. Rehman, K. Kan, L. Li, K. Shi, *J. Mater. Sci.* 52 (2017) 3757–3770.
- [51] W. Wang, Q. Zhu, Q. Dai, X. Wang, *Chem. Eng. J.* 307 (2017) 1037–1046.
- [52] K. Ahn, D.S. Yoo, D.H. Prasad, H. Lee, Y. Chung, J. Lee, *Chem. Mater.* 24 (2012) 4261–4267.
- [53] Y. Liu, C. Wen, Y. Guo, G. Lu, Y. Wang, *J. Phys. Chem. C* 114 (2010) 9889–9897.
- [54] H. Song, U.S. Ozkan, *J. Phys. Chem. A* 114 (2010) 3796–3801.
- [55] Q. Wang, B. Zhao, G. Li, R. Zhou, *Environ. Sci. Technol.* 44 (2010) 3870–3875.
- [56] Y. Xie, C. Li, L. Zhao, J. Zhang, G. Zeng, X. Zhang, W. Zhang, S. Tao, *Appl. Surf. Sci.* 333 (2015) 59–67.
- [57] P. Wang, S. Su, J. Xiang, H. You, F. Cao, L. Sun, S. Hu, Y. Zhang, *Chemosphere* 101 (2014) 49–54.
- [58] J. Zhang, H. Kumagai, K. Yamamura, S. Ohara, S. Takami, A. Morikawa, H. Shinjoh, K. Kaneko, T. Adschiri, A. Suda, *Nano Lett.* 11 (2011) 361–364.
- [59] G. Pantaleo, V. La Parola, F. Deganello, R.K. Singha, R. Bal, A.M. Venezia, *Appl. Catal. B-Environ.* 189 (2016) 233–241.
- [60] H. Li, L. Zhu, S. Wu, Y. Liu, K. Shih, *Int. J. Coal Geol.* 170 (2017) 69–76.
- [61] S. Qiao, J. Chen, J. Li, Z. Qu, P. Liu, N. Yan, J. Jia, *Ind. Eng. Chem. Res.* 48 (2009) 3317–3322.
- [62] E.J. Granite, H.W. Pennline, R.A. Hargis, *Ind. Eng. Chem. Res.* 39 (2000) 1020–1029.
- [63] Z.S. Wei, Y.W. Luo, B.R. Li, Z.Y. Chen, Q.H. Ye, Q.R. Huang, J.C. He, *J. Ind. Eng. Chem.* 24 (2015) 315–321.
- [64] H. Li, S. Wang, X. Wang, N. Tang, S. Pan, J. Hu, *Fuel* 202 (2017) 470–482.
- [65] C.L. Senior, *J. Air Waste Manag.* 56 (2006) 23–31.